ICARUS 97, 276–287 (1992)

High Resolution Surface Brightness Profiles of Near-Earth Asteroids

JANE X. LUU[1]

Harvard–Smithsonian Center for Astrophysics, 60 Garden Street, MS 52, Cambridge, Massachusetts 02138

AND

DAVID C. JEWITT

Institute for Astronomy, University of Hawaii

Received December 19, 1991; revised March 10, 1992

We present a new method to search for and estimate mass loss in near-Earth asteroids (NEAs) using high resolution surface photometry. The method was applied to 11 NEAs observed with a charge-coupled device (CCD) at the University of Hawaii 2.2-m telescope. The method yields limiting mass loss rates $\dot{M} \leq 0.1$ kg sec^{-1}, 1–2 orders of magnitude smaller than the typical rates of weakly active comets. However, these mass loss rate upper limits imply fractional active areas in NEAs that are comparable to cometary fractional active areas. Because of the small sizes of the NEAs, the mass loss rates produced by these fractional active areas are below the detection limit of current techniques; thus there may exist low-level cometary activity amongst the NEAs which goes unnoticed.

1. INTRODUCTION

1.1 The Comet–Asteroid Distinction

It may appear at first glance that comets and asteroids have little in common besides being two major groups of small bodies in the solar system. The physical appearances of the two groups seem very different: asteroids are inert objects and almost always appear stellar, while comets are volatile-rich and are most commonly recognized by their diffuse comae. Besides their physical appearances, comets and asteroids also seem to share few dynamical characteristics. The average low-eccentricity, low-inclination asteroidal orbits between Mars and Jupiter bear little resemblance to the eccentric, chaotic cometary orbits (Froeschlé 1990). It thus seems that a connection between comets and asteroids may be far-fetched, but recent advances in both observational and theoretical work suggest that this connection may not be as far-fetched as it might appear.

The distinction between comets and certain asteroids becomes less clear when we consider that comets can appear stellar and that several comets have been misclassified as asteroids in the past. For example, Comet Parker–Hartley was first identified as Asteroid 1986 TF (Nakano 1989), and the "Asteroid" 2060 Chiron now displays a resolved coma (e.g., Meech and Belton 1989, Luu and Jewitt 1990a). Volatiles, the usual signature of comets, are also present in some asteroids: the 3-μm water band has been identified in Asteroid 1 Ceres (Lebofsky *et al.* 1981) and other asteroids (Jones 1988). However, this is bound water, not free surface ice. Similarly, the dynamical distinction between comets and asteroids is also blurred. Wisdom (1987) has shown that chaos is not strictly reserved for cometary orbits and can also be found in the asteroid belt. In the outer belt, a number of asteroids and comets have similar orbits (Rickman 1988), and at the edge of the inner belt, many near-Earth asteroids (NEAs) exhibit comet-like orbital characteristics. For example, the orbit of NEA 2212 Hephaistos is similar to that of Comet P/Encke (Hahn and Rickman 1985). The reader is referred to Table III of Weissman *et al.* (1989) for a list of asteroids with comet-like characteristics.

Thus, thanks to observational and theoretical advances in the last decade, the distinction between comets and asteroids is no longer as clear cut as once it was. With some asteroids, the reported lack of a coma does not guarantee that the objects are not comets: 2060 Chiron was long suspected to be a comet before its coma was observed. In addition to the transient nature of coma in some comets, it is true that presence or absence of a coma

[1] To whom correspondence should be addressed.

0019-1035/92 $5.00

has been determined only *qualitatively*. As a result, the detection of coma depends strongly on the method and sensitivity of the particular observation.

As alternatives to direct imaging, other methods have been developed to decide whether an object is a comet or an asteroid. One method is to search for gaseous emission lines in asteroid spectra (Degewij 1980, Cochran *et al.* 1986). However, it is well known that optical spectra of active comets frequently show strong continua devoid of detectable gaseous emissions (e.g., P/Tempel 2, Spinrad *et al.* 1979 and Jewitt and Luu 1989), suggesting that conventional optical spectroscopy is not always the optimum way to establish cometary activity.

Another method is to check for nonasteroidal photometric behavior. The brightness of an asteroid in scattered light should scale in proportion to $f(\alpha)R^{-2}\Delta^{-2}$, where R is the heliocentric distance, Δ is the geocentric distance, and $f(\alpha)$ is the phase function; any deviation from this behavior would be suggestive of a variable coma around the asteroid. This method has been successfully applied to 2060 Chiron (e.g., Hartmann *et al.* 1990). Unfortunately, since it involves making observations over a significant fraction of the orbit of the asteroid, the long-term photometry method is very time consuming. Furthermore, if the observations are made at large phase angles, as is likely to be the case of the NEAs, the phase function becomes quite significant. Without prior knowledge of the phase function, it is not possible to correct for phase darkening in the asteroid photometry, making it difficult to judge whether the photometric behavior of the object is, in fact, asteroidal.

It is also natural to consider speckle interferometry as an alternative method, and indeed, speckle interferometry has been used in high resolution studies of several large asteroids (Drummond and Hege 1989). However, the speckle method is limited to the study of bright objects ($m_V \leq 14$), and is thus inapplicable to a majority of the NEAs.

1.2. This Work

In this paper, an independent method is described which will allow us to search for faint comae and so to estimate the mass loss rates in asteroids. The method is based on the direct comparison of high resolution asteroid surface brightness profiles with star profiles. All but the largest asteroids are unresolved. If an asteroid profile appears broader than a star profile, this indicates the presence of a coma, signifying mass loss.

Because of their comet-like orbits and their close approaches to the Sun, we deem the NEAs to be the most promising candidates for "comets in disguise," and we have begun a survey to search for faint comae around NEAs. The survey consists of taking high resolution images of NEAs and comparing their profiles with star profiles. The measured profiles are interpreted by means of a model which allows us to estimate the mass loss rate if coma is detected, and to place upper limits otherwise. The results are compared with mass loss rates from known cometary nuclei. The main advantages of the profile method are (1) it is simple, efficient, versatile, and (as we will show) can be very sensitive if the seeing is good; (2) it can be applied to asteroids as faint as 18th magnitude (compared to 14th for the speckle method); (3) it exploits the excellent seeing (typically <1 arcsec) on Mauna Kea, where all the observations were made; and (4) it yields quantitative parameters with which to compare comets and asteroids observed in identical fashion. The observations are discussed in Section 2, the model in Section 3, and the interpretation of the profiles in Section 4. In Section 5, the likelihood of detecting cometary activity in NEAs is estimated.

TABLE I
NEA Observation Log

NEA	UT date	R [AU]	Δ [AU]	α [°]	m_V[a]
1917	1989 08 18	1.29	0.44	43.1	15.5
	1989 08 19	1.28	0.44	43.3	15.4
2059	1989 08 22	1.27	0.95	51.7	16.8
	1989 08 23	1.27	0.94	51.8	16.8
2122	1989 08 18	2.33	1.46	15.9	15.5
	1989 08 22	2.33	1.43	14.4	15.4
2744	1989 08 22	1.55	0.65	26.7	16.2
	1989 08 23	1.55	0.65	26.3	16.1
3200	1989 08 19	1.61	1.48	37.9	17.9
	1989 08 22	1.64	1.47	37.4	17.9
3362	1989 08 19	1.24	0.53	51.7	18.8
	1989 08 24	1.27	0.51	49.3	18.7
3753	1989 08 20	1.48	0.88	41.6	17.1
	1989 08 22	1.48	0.86	41.5	17.0
(4257) 1987 QA	1989 08 19	1.70	0.77	20.3	17.0
	1989 08 20	1.69	0.76	20.0	16.9
1989 JA	1989 08 23	1.75	1.07	70.0	17.2
	1989 08 25	1.68	1.08	68.5	17.2
1989 OB	1989 08 18	1.29	0.29	16.4	15.2
	1989 08 19	1.29	0.29	16.9	15.1
(4769) 1989 PB	1989 08 18	1.07	0.07	32.8	12.5
	1989 08 20	1.05	0.05	37.6	12.0
	1989 08 22	1.04	0.04	49.2	11.5

[a] Estimated from m_V (1,1,0).

2. OBSERVATIONS

2.1. Instrumentation

We obtained high resolution profiles of 11 NEAs in the time period UT 1989 August 18–25; a log of the observations is shown in Table I. We selected as our targets those

NEAs which had the smallest R, in our observing window. Since R and Δ are interdependent, minimizing R also yields small Δ, which is desirable for high spatial resolution. The profiles were extracted from CCD images taken with the University of Hawaii (UH) 88-inch telescope on Mauna Kea. The detector used was a 416 × 580 pixel GEC CCD camera situated at the $f/10$ Cassegrain focus, giving an image scale of 0.20 arcsec/pixel.

The main attributes of the GEC are its low readout noise (~6 electrons) and high linearity, rendering the images easy to "flatten." The "flattening" process removes sensitivity variations in the individual pixels and includes subtraction of the bias (zero exposure) frames from the images, then division of the images by the "flat field" frames. The bias frames were taken throughout the night as an insurance against large fluctuations in the bias level; however, it was subsequently found that the bias level was constant to 0.2% throughout the observing run. Images of the morning twilight sky were taken after each night and the nightly "flat field" frame was computed from the median of these frames. After flattening, the images were uniform in sensitivity at the ±0.5% level across the CCD.

All observations were obtained using a broadband Mould R filter under photometric conditions and subarcsecond seeing. The R filter is near the wavelength of peak quantum efficiency (~0.4) of the GEC CCD. It provides maximum sensitivity to extended emission from possible faint coma. Since a typical NEA has a radius on the order of 1 km (10^{-3} arcsec at Δ = 1 AU), it is not possible to resolve the NEAs, and we only hope to detect comae that extend beyond the seeing disk. The telescope was tracked at sidereal rate for all asteroids. We tracked the telescope at sidereal rate instead of asteroidal rates because the UH 88-inch could not (at the time) guide with sufficient accuracy and uniformity in nonsidereal mode. Each NEA was imaged at least twice on at least two different nights as a check on the repeatability of the measured profiles. The integration times were typically 5–8 min, such that the asteroid trails were ≤5 arcsecs (25 pixels) in length. The presence of field stars within each CDD image was extremely important, since the profile method depends on the comparison of an asteroid profile with a star profile. The position of the field stars on the CCD image was not important as the point spread function (PSF) was invariant with respect to position across the CCD. The NEAs were positioned on the CCD image in such a way as to include field stars in each frame, with the typical asteroid–field star separation <50 arcsec. To be suitable for later comparison, the field stars were chosen to be at least as bright as the NEAs, but not bright enough to saturate the CCD chip. If no suitable star could be found near an NEA, that NEA was ignored until its motion carried it into the vicinity of a suitable star.

2.2 Near-Earth Asteroid Profiles

In each image, the brightest nonsaturated star nearest to the NEA trail was selected as the primary reference star. The background sky around the star was measured and subtracted from the image. As the GEC was very linear and the field of view was not large (~1′ × 2′), the background sky around the reference star was representative of the background sky on the rest of the chip.

To obtain the asteroid profile, each image was rotated using a fifth order polynomial interpolation so that the asteroid trail was aligned parallel to the pixel rows on the CCD chip. Profiles of the NEAs and their reference stars were then obtained by averaging along the rows. Each star profile was averaged over the entire width of the star and each NEA profile averaged over the entire length of the NEA trail. Both profiles were then normalized and plotted on a single graph to search for any dissimilarities between the two profiles. Figure 1 shows log-linear profiles of the 11 observed NEAs, superimposed upon the profiles of the reference stars. A few images show large scatter in the sky background (visible as large "spikes" or "dips"), due to cosmetic imperfections in the CCD or low signal-to-noise. It is seen that most NEA profiles are very similar to their reference star profiles within the central 2″ where most of the light is contained; there is no clear indication of comae, although there are some profiles with tantalizingly broad wings, such as in 1917 Cuyo, 3362 Khufu, and 1989 JA. In the cases of these NEAs, we examined carefully their profiles taken on other nights to verify the suggestion of coma. In no case did we find reproducible, unambiguously broadened profiles. We thus conclude that no coma was detected in any of the observed NEAs.

3. SURFACE BRIGHTNESS MODEL

We interpret the measured profiles using seeing-convolved images of model comets. We create images of model comets which possess the same image scale and PSF as the data, so that model profiles and real profiles can be compared directly. The steps involved in creating model profiles are (1) creation of a coma in an artificial image, (2) creation of a nucleus in the middle of the coma, and (3) convolution of the model images with the seeing. The details are as follows.

3.1. Simulation of the Coma

In our models, it is assumed that the coma is spherically symmetric and in steady-state, i.e., the surface brightness of the coma is $B(r) = K/r$, where K is a constant of

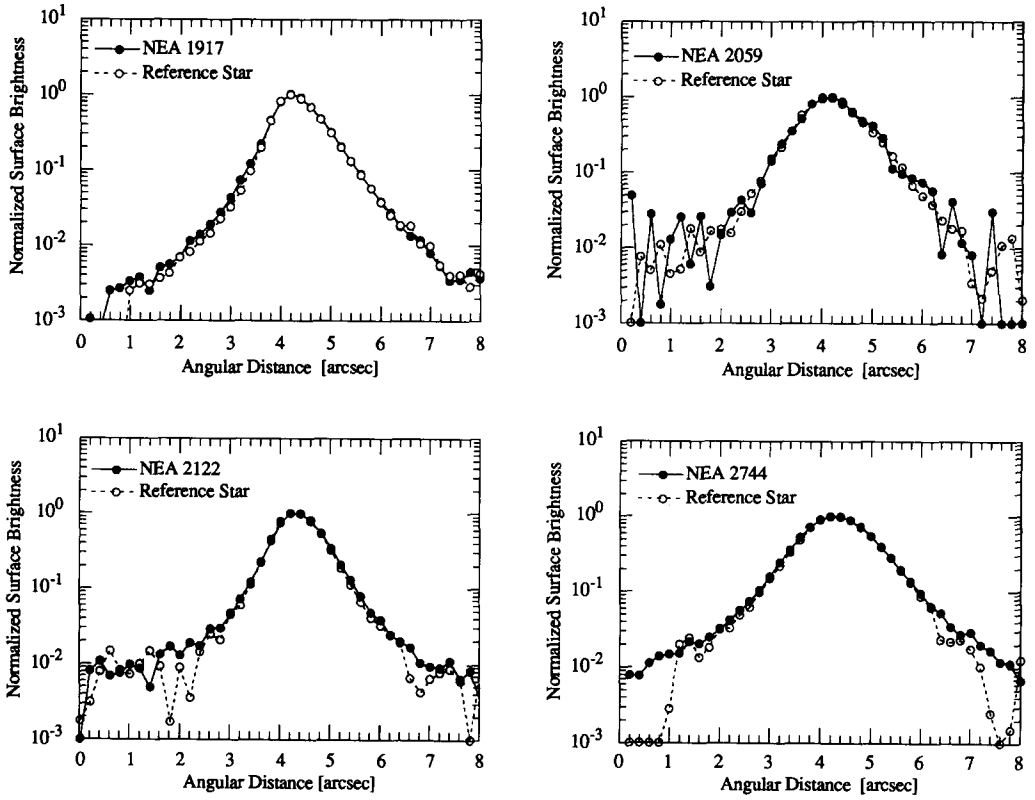

FIG. 1. The logarithm of the surface brightness is plotted versus linear distance in the plane of the sky (in arcsec) for 11 NEAs and their reference stars. The surface brightness is normalized to unity at the peak of each profile.

proportionality and r is the impact parameter measured from the nucleus in the plane of the sky. The model images are 100 × 100 pixels in size, with the point-source nucleus located at the central pixel [pixel (50, 50)]. Each pixel subtends 0.2″ × 0.2″, as in the data. From the $1/r$ surface brightness dependence, the intensity I of each pixel in the coma is determined by the integral

$$I = \int_{y_1}^{y_2}\int_{x_1}^{x_2} \frac{K}{\sqrt{x^2 + y^2}}\,dx\,dy, \tag{1}$$

where x_1, x_2 are the left and right edges of a pixel, respectively, and y_1 and y_2 are the lower and upper edges, respectively. Equation (1) has the solution

$$\begin{aligned}\int_{y_1}^{y_2}\int_{x_1}^{x_2} &\frac{K}{\sqrt{x^2 + y^2}}\,dx\,dy \\ &= K\{y_2 \ln(x_2 + \sqrt{x_2^2 + y_2^2}) + x_2 \ln(y_2 + \sqrt{x_2^2 + y_2^2}) \\ &\quad - y_2 \ln(x_1 + \sqrt{x_1^2 + y_2^2}) - x_1 \ln(y_2 + \sqrt{x_1^2 + y_2^2}) \\ &\quad - y_1 \ln(x_2 + \sqrt{x_2^2 + y_1^2}) - x_2 \ln(y_1 + \sqrt{x_2^2 + y_1^2}) \\ &\quad + y_1 \ln(x_1 + \sqrt{x_1^2 + y_1^2}) + x_1 \ln(y_1 + \sqrt{x_1^2 + y_1^2})\}. \end{aligned} \tag{2}$$

Using Eq. (2), each coma pixel was assigned the proper intensity. This procedure was carried out identically for every model image.

3.2. *Simulation of the Nucleus*

Successive preconvolution models were distinguished from one another by the parameter η, defined as the ratio of the coma cross-section C_c to the nucleus cross-section C_n:

$$\eta = \frac{C_c}{C_n} = \frac{I_c}{I_n}, \quad \eta \geq 0. \tag{3}$$

I_c is the flux density scattered by the coma, and I_n is the flux density scattered by the nucleus. I_c is determined from aperture photometry on the model coma. The parameter η can take on the values $\eta \geq 0$, with $\eta = 0$ corresponding to a bare nucleus. The reference photometry aperture radius used is 1 arcsec. As can be seen in Fig. 2, this aperture is sufficiently large to take in most (86%) of the light in our NEA images, given the ≤1 arcsec seeing.

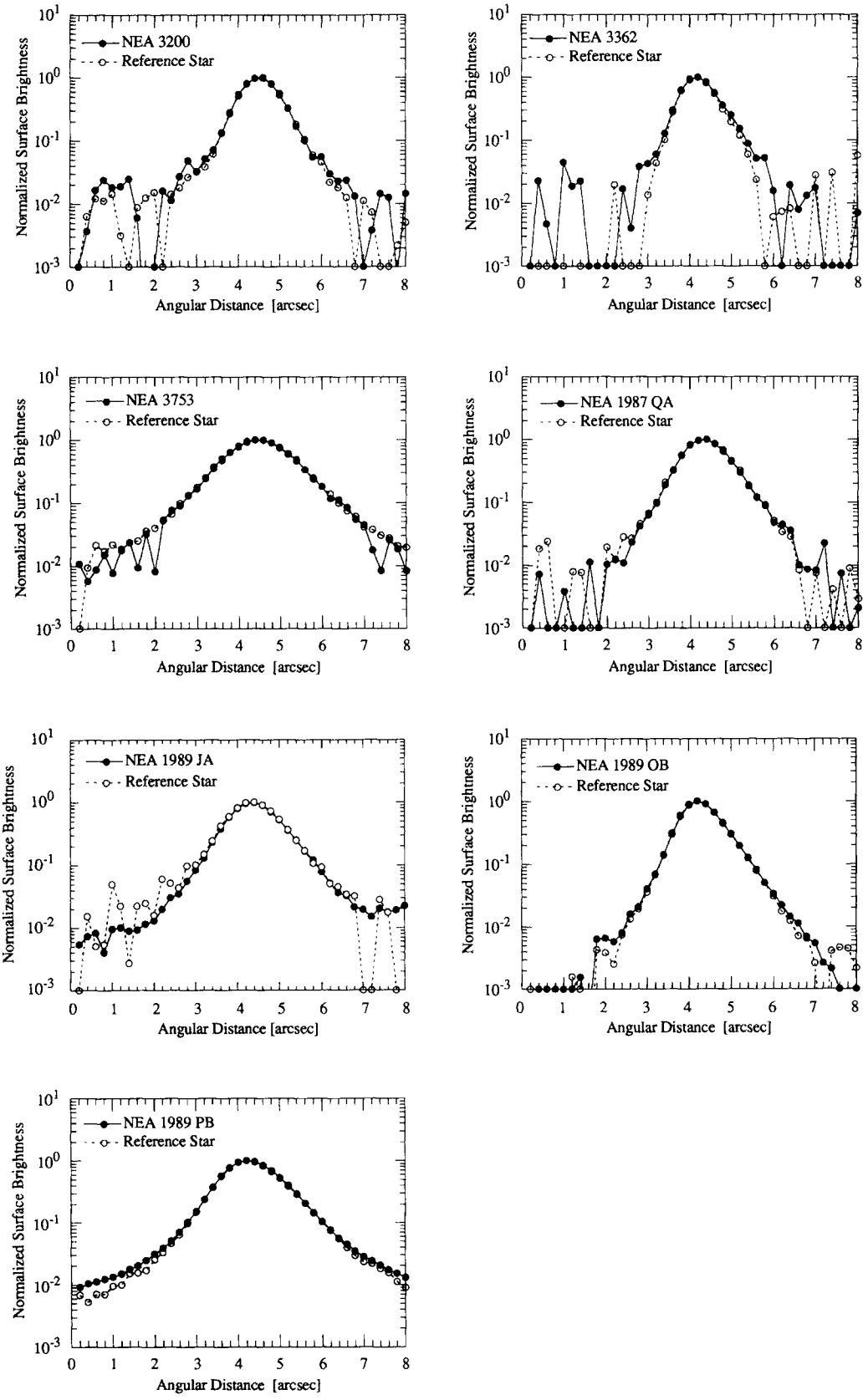

FIG. 1—*Continued*

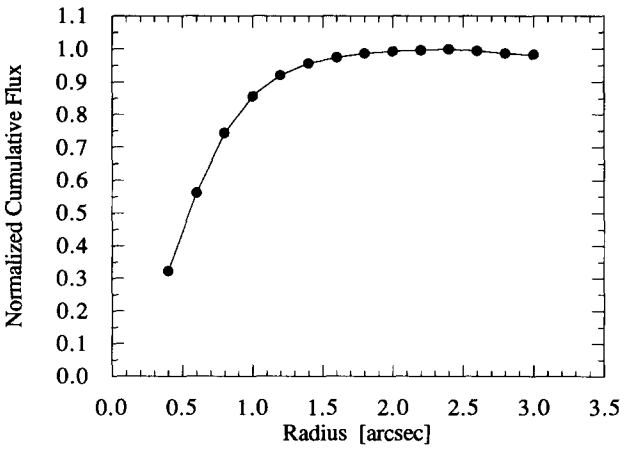

FIG. 2. The normalized cumulative flux of a field star as a function of radial distance. In this example, 86% of the light falls within a 1-arcsec radius.

3.3. *Convolution of Model Images*

Astronomical images are blurred by atmospheric turbulence (the seeing), and by imperfections in the telescope and detector optics. In order to compare a model profile with a real object profile, the blurring of the original image must be accounted for, either by (1) convolving the model with the seeing, to simulate the conditions under which the image was taken, or (2) deconvolving the blurred image to take away atmospheric and instrumental effects. We favor convolution over deconvolution because the latter tends to amplify noise in the image, rendering the deconvolved image difficult to interpret. The result of convolution is the blurring of the model image, similar to the way light from the original point source has been blurred on its way to the telescope focal plane. The amount of "blurring" is represented in the PSF of the image, which is obtained from field stars. For each NEA image, a primary reference star in the field is selected as the PSF. Model images are then convolved with this PSF, producing model profiles which can be directly compared with the NEA profile.

We find that our convolved models are very reliable in reproducing the image shape, as demonstrated by Figs. 3a and 3b. Both figures show that the convolved model profiles (characterized by $\eta = 0$, as appropriate for a point source) are identical to the stellar profiles, proving that the model profiles can be compared with real NEA profiles with confidence.

The accuracy in η is dependent on the resolution of the data and the signal-to-noise of the image. With high signal-to-noise profiles taken under good seeing, we are capable of distinguishing profiles with the resolution $\Delta\eta = 0.01$. In other words, the profile fitting technique applied to high signal-to-noise surface photometry is capable of revealing a coma with a cross section of ~1% of the nucleus cross section. This is illustrated by Fig. 4, where a series of models separated by $\Delta\eta = 0.01$ are shown. The models in Fig. 4 have been convolved with the typical Mauna Kea seeing to simulate profiles from actual images. The figure shows that, as η increases, the profile is broadened, reflecting the increasing fraction of coma. The model profiles in the figure are clearly distinguishable, providing evidence for our resolution of $\Delta\eta = 0.01$.

3.4. *Interpretation of the Model Profiles*

The mass loss rate can be expressed as a function of the parameter η. The total scattering cross-section of coma grains C_c within an aperture of radius d is

$$C_c = \int_{a_{min}}^{a_{max}} Q_s \pi a^2 n(a)\, da, \tag{4}$$

and the mass of the coma M_c in an aperture of the same radius d is

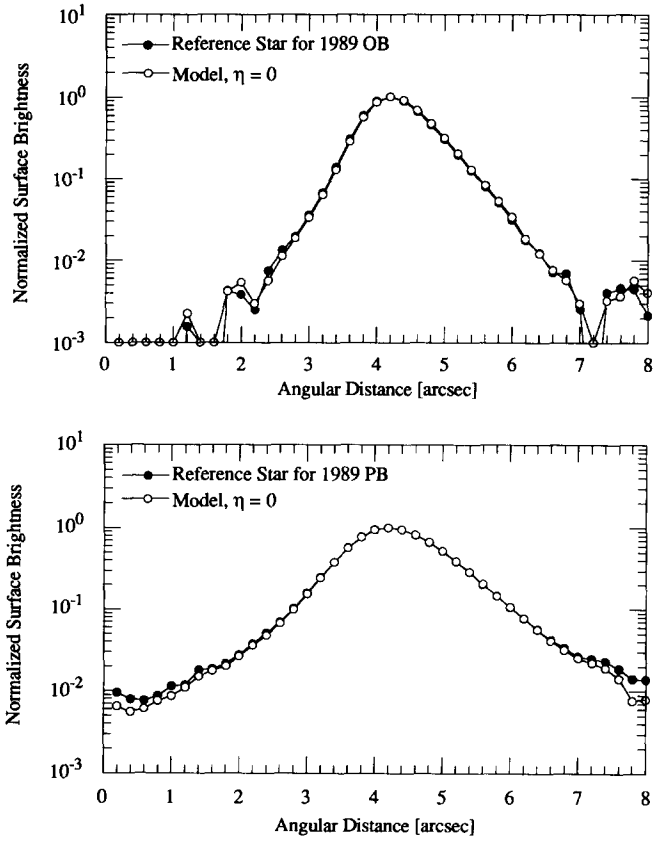

FIG. 3. (a) Profiles of a model (characterized by $\eta = 0$) and of the reference star for 1989 OB. The model profile is identical to that of the star, showing that our convolution method is reliable. (b) Same as (a), but for 1989 PB.

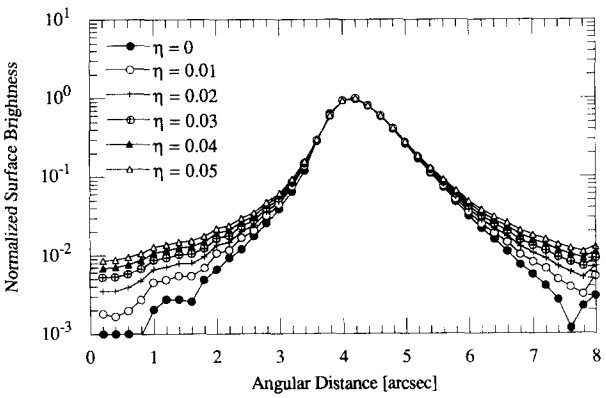

FIG. 4. Model profiles as a function of η. The coma in the model has a $1/r$ surface brightness. The models have been convolved with the seeing to simulate actual profiles as described in Section 3.

$$M_c = \int_{a_{min}}^{a_{max}} \frac{4\pi\rho a^3 n(a)\, da}{3}. \tag{5}$$

In both Eqs. (4) and (5), a is the grain radius, $n(a)\, da$ is the differential grain size distribution, and a_{min} and a_{max} are the minimum and maximum grain radii, respectively. Q_s is the scattering efficiency, and ρ is the grain density. The cross-section weighted mean grain radius for scattering is

$$\bar{a} = \frac{\int_{a_{min}}^{a_{max}} Q_s \pi a^3 n(a)\, da}{\int_{a_{min}}^{a_{max}} Q_s \pi a^2 n(a)\, da}. \tag{6}$$

Particles with $\bar{a} \ll \lambda$ will be inefficient scatterers of optical radiation while those with $\bar{a} > \lambda$ are rare. In the absence of detailed knowledge of the scatterers, we adopt $\bar{a} \sim \lambda$, assuming $Q_s \sim 1$, and the coma mass can be rewritten as

$$M_c = \frac{4\rho\bar{a}C_c}{3}. \tag{7}$$

The mean mass loss rate is then M_c/τ_d, where τ_d is the diaphragm crossing time. Assuming the Bobrovnikoff–Delsemme speed v_{BD} for the grain speed (Delsemme 1982), τ_d can be written

$$\tau_d \sim 1250\, d\, \Delta R^{0.5} \quad [\mathrm{s}]. \tag{8}$$

In Eq. (8), d [arcsec] is the angular radius of the photometry diaphragm, and Δ and R are in AU. Since it is a molecular outflow speed, the Bobrovnikoff–Delsemme speed is an upper limit to the true speed of the coma dust particles, thus usage of v_{BD} gives a robust lower limit to τ_d and a strong upper limit to the derived mass loss rate. The mass loss rate $\dot{M}_c$ can then be written

$$\dot{M}_c = \frac{(4/3)\rho\bar{a}C_c}{1250\, dR^{0.5}\Delta} \quad [\mathrm{kg\ sec^{-1}}]. \tag{9}$$

Making use of Eq. (3) and equating $C_n = \pi r_{NEA}^2$, the mass loss rate has the final form

$$\dot{M}_c = \frac{1.1 \times 10^{-3}\, \pi\rho\bar{a}\eta r_{NEA}^2}{dR^{0.5}\Delta}. \tag{10}$$

4. INTERPRETATION OF NEA PROFILES

Comparison with star profiles (Fig. 1) showed that there was no clear evidence for mass loss in the observed NEAs. This empirical result is confirmed when NEA profiles are fitted with model profiles: the $\eta = 0$ models provide a good fit to all NEAs. We can thus place an upper limit, η_{lim}, by identifying the largest $\eta > 0$ that is still consistent with the NEA profile. This is done by minimizing the χ^2 values when comparing the $\eta > 0$ models with the NEA profiles; the errors in η_{lim} are also calculated from the χ^2 values. This fitting method is finally verified by eye.

The mass loss rate $\dot{M}$, or its upper limit $\dot{M}_{lim}$, can be calculated by simply substituting the appropriate value of η or η_{lim} into Eq. (10); the results are presented in Table II. The values of $\dot{M}$ in Table II were computed with $\bar{a} = 0.5 \times 10^{-6}$ m, $\rho = 1000$ kg m^{-3}, $d = 1$ arcsec. The table shows that $\dot{M} \leq 0.1$ kg sec^{-1}, which is $10^5\times$ smaller than the mass loss rate from P/Halley at perihelion, and 1–2 orders of magnitude smaller than the typical mass loss rates of the known low-activity comets (see Table III for a list of cometary mass loss rates).

It is interesting to compare our detection limits with those obtained using a spectroscopic technique by Cochran *et al.* (1986). For this purpose, we must convert the Cochran *et al.* CN column densities to total dust mass loss rates. The dust-to-gas ratio is typically of order unity (e.g., $\mu = 2 \pm 1$ for P/Halley, McDonnell *et al.* 1991), and is assumed to be unity here. The conversion is accomplished using

$$\dot{M} = \frac{n_{CN}\Delta^2 d^2 m_{CN}}{\tau_d f_{CN}}. \tag{11}$$

In Eq. (11), n_{CN} is the CN column density, m_{CN} is the CN molecular mass, and f_{CN} is the fractional abundance of CN. τ_d can be found from Eq. (8), and f_{CN} is assumed to be ~0.2% (Schloerb *et al.* 1986). The diaphragm radius used by Cochran *et al.* was 4 arcsec (Cochran, personal

TABLE II
NEA Mass Loss Rates and Fractional Active Areas

NEA	R [AU]	Δ [AU]	r^a [km]	η	$\dot{M}_c{}^b$ [kg sec^{-1}]	$F_{act}{}^c$
1917	1.29	0.44	1.5	$\leq 0.01 \pm 0.02$	≤ 0.07	$\leq 0.6 \times 10^{-4}$
2059	1.27	0.95	2.0	$\leq 0.01 \pm 0.004$	≤ 0.06	$\leq 0.3 \times 10^{-4}$
2122	2.33	1.46	6.5	$\leq 0.01 \pm 0.01$	≤ 0.30	$\leq 3.0 \times 10^{-4}$
2744	1.55	0.65	1.5	$\leq 0.02 \pm 0.007$	≤ 0.09	$\leq 1.5 \times 10^{-4}$
3200	1.61	1.48	1.5	$\leq 0.01 \pm 0.01$	≤ 0.02	$\leq 3.5 \times 10^{-5}$
3362	1.24	0.53	0.5	$\leq 0.1 \pm 0.04$	≤ 0.07	$\leq 4.8 \times 10^{-4}$
3753	1.48	0.88	2.0	$\leq 0.01 \pm 0.007$	≤ 0.06	$\leq 4.6 \times 10^{-5}$
1987 QA	1.70	0.77	1.5	$\leq 0.01 \pm 0.004$	≤ 0.04	$\leq 0.9 \times 10^{-4}$
1989 JA	1.75	1.07	1.0	$\leq 0.01 \pm 0.01$	≤ 0.01	$\leq 6.7 \times 10^{-5}$
1989 OB	1.29	0.29	1.0	$\leq 0.01 \pm 0.01$	≤ 0.05	$\leq 1.0 \times 10^{-4}$
1989 PB	1.07	0.07	0.5	$\leq 0.01 \pm 0.01$	≤ 0.08	$\leq 3.5 \times 10^{-4}$

[a] Estimated from m_V (1,1,0), assuming albedo $p = 0.1$.
[b] From Eq. (10), assuming $\bar{a} = 0.5 \times 10^{-6}$ m, $\rho = 1000$ kg m^{-3}, and $d = 1$ arcsec.
[c] From Eq. (13).

communication). The Cochran limits were found to be 2–10× larger than those presented in Table II, proving the sensitivity of the profile method.

Knowledge of $\dot{M}$ can be used to derive another useful parameter: the fractional active area on the surface of the NEA. Assuming that, if volatiles exist, the main volatile is water ice, the active area A_{act}[m^2] is

$$A_{act} = \frac{\dot{M}}{\mu Z_w}, \tag{12}$$

where μ is the dust-to-gas ratio, Z_w [kg m^{-2} sec^{-1}] is the mass flux of water, and the fraction of active area, F_{act}, is A_{act} divided by the total surface area:

$$F_{act} = \frac{\dot{M}}{4\pi r_{NEA}^2 \mu Z_w}. \tag{13}$$

The dust-to-gas ratio μ is again assumed to be 1, and Z_w for the NEAs can be found from the familiar heat balance equation,

$$\frac{F_{Sun}(1 - A)}{4R^2} - \varepsilon\sigma T^4 = L(T)\, Z(T), \tag{14}$$

where F_{Sun} [W m^{-2}] is the solar constant, A is the albedo, T is the temperature [K], and L [J kg^{-1}] is the latent heat. The factor of 4 in the first term of Eq. (14) is appropriate for an isothermal, fast rotator. This assumption tends to

TABLE III
Cometary Mass Loss Rates and Fractional Active Areas

Comet	r_{nuc} [km]	$\dot{M}$ [kg sec^{-1}]	F_{act}	References[a]
P/Encke	3.1[b]	89 (R = 0.90 AU)	0.04	1, 2
P/Arend-Rigaux	5.2	6.1 (R = 1.58 AU)	1.6×10^{-4}	3, 4
P/Neujmin 1	10.4	6.1 (R = 1.68 AU)	2.3×10^{-4}	5, 6
P/Tempel 2	5	43 (R = 1.65 AU)	1.3×10^{-3}	7, 8
P/Halley	5.6	100 (R = 2.8 AU)	0.1	9
P/Schwassmann-Wachmann 1	20	10 (R = 5.8 AU)	0.06	10

[a] References: (1) Luu and Jewitt (1990b), (2) A'Hearn *et al.* (1985), (3) Millis, A'Hearn, and Campins (1988), (4) Jewitt and Meech (1985), (5) Jewitt and Meech (1988), (6) Campins *et al.* (1987), (7) Jewitt and Luu (1989), (8) A'Hearn *et al.* (1989), (9) Keller *et al.* (1987), and (10) Jewitt (1990).
[b] The radius was calculated from the cross-section assuming a 5% albedo for the nucleus.

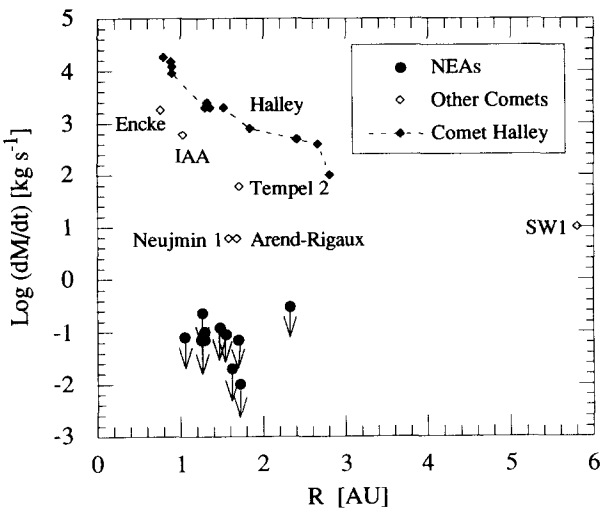

FIG. 5. Derived mass loss rates, $\dot{M}$, for well studied comets and the observed NEAs plotted as a function of heliocentric distance R. Downward arrows denote upper limits (for the NEAs). The cometary $\dot{M}$ are clearly distinguished from the upper limits for NEAs, as expected.

underestimate the surface area needed to produce a given mass loss rate. It thus provides an intentionally generous estimate of the limiting F_{act}. The calculated limiting F_{act} for the observed NEAs can be found in Table II; they are on the order of $\leq 10^{-4}$, or $\leq 0.01\%$ of the surface area.

5. COMPARISON WITH COMETS

It is interesting to compare the upper limits for $\dot{M}$ and F_{act} in NEAs with the values of $\dot{M}$ and F_{act} in known comets (sample values are listed in Table III). In graphical form, Fig. 5 shows the NEA and cometary mass loss rates plotted vs R, while Fig. 6 shows the NEA and cometary fractional active areas vs R. Notice that, in Fig. 5, the NEA $\dot{M}_{lim}$ values are well below the cometary $\dot{M}$. Figure 5 quantifies the evident difference between the NEAs and the low-activity comets: as expected, the NEAs lose mass less rapidly then comets by at least 1 order of magnitude. However, when fractions of an active area are compared, Fig. 6 shows that the NEA upper limits for F_{act} are comparable to F_{act} for the low-activity comets P/Arend–Rigaux and P/Neujmin 1 (and to a lesser extent, P/Tempel 2 and P/Schwassmann–Wachmann 1). The implication of Fig. 6 is that some of the NEAs *could* have fractional active areas that are comparable to the fractional active areas on low-activity comets, but their small sizes ($r_{NEA} \sim 1$–3 km as opposed to $r_{comet} \sim 5$–10 km) give rise to mass loss rates too small to be detectable with current techniques.

According to this viewpoint, size may be a significant influence on whether an object is classified as a low-activity comet or an NEA: weakly active comets are more likely to be classified as such if their nuclei are large, while small, weakly active objects may well exist unnoticed amongst the NEAs. Thus, Fig. 6 strengthens the hope that it may be possible one day to detect cometary activity in NEAs and settle the issue of comets evolving into NEAs. In Table IV, we calculate how large a comet nucleus needs to be in order for its mass loss rate to be detected, using a mass loss rate detection limit of $\dot{M} = 0.1$ kg sec^{-1}, compatible with the present data. In the vicinity where NEAs are often observed ($R \sim 1$ AU), if we assume $F_{act} \sim 10^{-4}$ (as in P/Arend-Rigaux and P/Neujmin 1), the minimum size for a detectable coma is $r_{crit} \sim 1$ km, the average size of an NEA. If $F_{act} < 10^{-4}$, the comets would need to be larger than the average NEA for coma to be detected.

5.1. *Size Bias in Cometary Nucleus Observations*

If we make the ad hoc assumption that unknown mechanisms limit F_{act} on low-activity comets to 10^{-4}–10^{-5}, then Fig. 6 also suggests a very simple explanation for the fact that most comet nuclei studied to date are on the order of a few km in radius or larger. At $R = 1$ AU, comets with $F_{act} = 10^{-4}(10^{-5})$ need to be larger than the critical size $r_{crit} \sim 1(3)$ km in order to be classified as comets when present observational techniques are used: smaller ones are not capable of producing detectable comae and so either are labeled as "asteroids" or go undetected.

6. REACTIVATION OF EXTINCT COMETS

An object classified as an NEA could exhibit mass loss under two circumstances: (1) it is a very weakly active

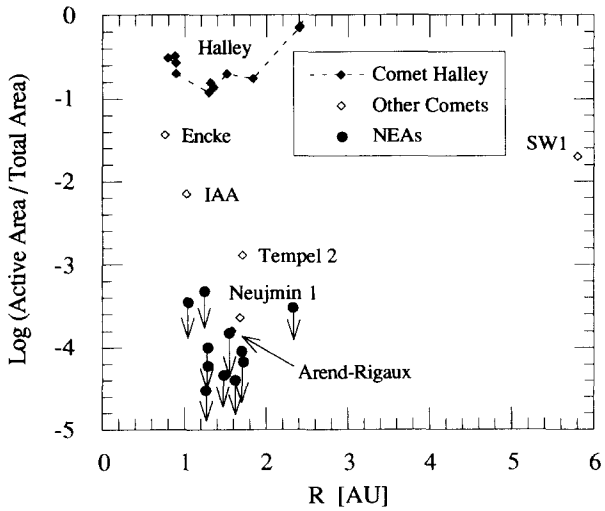

FIG. 6. Fractional active areas for comets and observed NEAs, plotted as a function of heliocentric distance R. Downward arrows denote upper limits. The NEAs and comets now more nearly overlap, compared to Fig. 5.

TABLE IV
Critical Radius for Detectable Mass Loss Rate

F_{act}	r_{crit}[a] [km]	F_{act}	r_{crit}[a] [k]
R = 1 AU		R = 2 AU	
10^{-1}	0.03	10^{-1}	0.1
10^{-2}	0.1	10^{-2}	0.3
10^{-3}	0.3	10^{-3}	1.0
10^{-4}	0.9	10^{-4}	3.2
10^{-5}	3.0	10^{-5}	10.1

[a] r_{crit} was calculated according to Eq. (10), assuming a 5% albedo and a detection limit M = 0.1 kg sec^{-1}.

comet which has evolved into an NEA orbit, but its mass loss rate is too small to be easily detected (see previous section, Section 5.1); or (2) it is an "extinct" comet which has been reactivated. The first circumstance has not been proven to occur, although dynamical studies have not ruled it out (Weissman *et al.* 1989); likewise, the second circumstance has not been confirmed. Complete mantling of the nucleus may be impossible due to porosity, or due to cracks in the surface produced by thermal stresses (Kührt 1984). If we assume that comets evolve into NEAs by complete mantle coverage, it is an interesting exercise to estimate the likelihood of detecting a reactivated comet.

Two obvious possibilities present themselves as mechanisms of reactivation:

(1) individual impacts that destroy part of the mantle so as to expose the volatiles underneath;

(2) mantle erosion due to micrometeoroid bombardment.

Undoubtedly, other mechanisms exist that can also create openings in the mantle; however, we restrict our discussion to the two mechanisms mentioned above because these processes are sufficiently understood that the basic physical parameters are established, allowing us to assess their likelihood as reactivation mechanisms. We also assume that, regardless of the reactivation mechanism, the length of the active period (the time it takes for the mantle to regrow and recover the active area) is sufficiently long that the nucleus has a chance of being observed while outgassing. Various models have suggested that mantle growth requires a timescale on the order of one to a few orbital revolutions (e.g., Fanale and Salvail 1984, Grün *et al.* 1989, Rickman *et al.* 1990), corresponding to perhaps 10 years of outgassing activity, once initiated.

The efficiencies of the two mechanisms listed above are estimated in the Appendix. The results of the calculations can be summarized as follows:

1. *Single-impact cratering.* For a 1-km radius NEA, the collision time for an impact large enough to produce a detectable coma is $\sim 3 \times 10^{13}$ sec or 1×10^6 years. If it takes 1–2 NEA orbital revolutions ($\sim$10 years) for the mantle to cover the surface, then the chance of witnessing this reactivation event is $10/10^6$ years, or 10^{-5}. Therefore, we would need to examine 10^5 NEAs in order to observe one such event—a daunting requirement, since the number of known NEAs is $\ll 10^5$.

2. *Microbombardment erosion.* Assuming an erosion rate similar to that of the moon, we calculate that a 5-cm-thick mantle can be eroded away in $\sim 5 \times 10^7$ years, or approximately an NEA lifetime. Given the long erosion time scale, it is unlikely that we will observe a comet reactivated by microbombardment erosion.

Based on our calculations, we conclude that detection of an impact-reactivated comet nucleus in an NEA orbit is not easily achieved, mostly because of the competition between the timescale for surface mantle coverage (short) and the timescale for reactivation (long). However, the detection of a very weakly (but continuously) active comet may be more feasible. The low-activity comet P/Encke is presently in an NEA-like orbit, suggesting that some low-activity comets can evolve dynamically into an NEA-like orbit. Figure 6 suggests that other Encke-like objects may exist among NEAs.

7. FUTURE WORK

In this paper, we have described a profile-fitting method that is sensitive to mass loss rates >0.1 kg/sec, when applied to kilometer-sized NEAs. For comparison, this is 4 to 5 orders of magnitude smaller than the mass loss rate from P/Halley when near perihelion (see Fig. 5). Profile-sitting is thus competitive with other techniques used to search for mass loss in asteroids, including spectroscopic searches published to date. Unfortunately, NEAs possessing fractional active areas similar to those of weakly active comets would fall at, or slightly beneath, the limits of detection of the existing methods. For example, the weakly active comets P/Arend-Rigaux and P/Neujmin 1 lose mass at about 10 kg/sec, but have surface areas about 100× larger than those of NEAs in our sample. Thus the present observations cannot be used to reject the hypothesis that some NEAs are outgassing from fractional active areas similar to those of weakly active comets.

Future profile measurements from Mauna Kea will benefit from several recent technical advances. First, new anti-reflection coated CCDs installed at the UH 2.2-m telescope have quantum efficiencies twice that of the GEC CCD used for the initial observations. Second, a new fast-response autoguider allows the telescope to be tracked with high accuracy at asteroidal rates, decreasing the area on the CCD from which the faint wings of the surface brightness profile must be recovered. Third, a new Casse-

grain secondary has been built to remove residual aberrations present in the 2.2-m primary. The telescope has recently given images better than 0.3″ FWHM, and the intensity in the wings of the images is significantly reduced. Together, these improvements will allow us to increase the sensitivity of the profile-fitting method to weak coma by more than 1 order of magnitude.

8. CONCLUSIONS

From high resolution surface photometry of NEAs, we conclude that:

(1) There was no compelling evidence for comae in the 11 observed NEAs (see Table II).

(2) The upper limits to allowed mass loss rates are of order

$$\dot{M} \leq 0.1 \text{ kg sec}^{-1},$$

which is 10–100× smaller than the typical rates reported in weakly active comets.

(3) The present application of the profile-fitting technique implies that we cannot exclude the existence of NEAs with fractional active areas comparable to the fractional active areas on low-activity comets. Thus, it is possible that some NEAs could be as active (per unit area) as are some comets, but the very small sizes of typical NEAs (radius ~1–3 km) may preclude their detection with current instrumentation.

(4) Likewise, low-activity comets need to be larger than ~ a few km in radius for their weak comae to be detected; smaller ones may go unnoticed or be classified as asteroids. This may in part explain the apparent underabundance of comet nuclei with radii <1 km.

APPENDIX

Reactivation Mechanisms for Comet Nuclei

1. Single-impact cratering. From impact craters on the surfaces of the planets and their planetary satellites, we know that impact cratering by meteoroids is common. We wish to determine what kind of impact is capable of removing a large enough piece of the mantle for cometary activity to be detectable, and on what timescale this takes place. Since the gravity of a 1-km-radius nucleus is very small, any ejecta produced by impact cratering is likely to escape from the surface (the escape velocity $v_e = 0.7$ m sec^{-1}). Based on the wealth of research on impact cratering, we can relate the kinetic energy of the projectile to the diameter of the resultant crater (Gault 1973, Gault 1974):

$$D = 1.342 = 10^{-5} \rho_P^{1.6} \rho_T^{-0.5} KE^{0.29} (\sin\theta)^{1/3},$$

where D is the diameter of the crater (m), ρ_P is the density of the projectile (kg m^{-3}), ρ_T is the density of the target (kg m^{-3}), KE is the kinetic energy of the projectile (J), and θ is the incident angle measured from the target surface. This result was derived from hypervelocity impact experiments on basalt, and is assumed to be roughly applicable for impact into a comet mantle. From Table II, we calculate that the active area needs to be ~ a few × 10^3 m^2 for the coma to be detected by the profile method. It we assume normal incidence ($\theta = 90°$), a projectile density and a target density $\rho_P = \rho_T = 1000$ kg m^{-3}, an active area $A = 3000$ m^2 ($D \sim 61.8$ m), and a projectile velocity $v_P = 30$ km/sec (as is appropriate for an object in orbit at $R \sim 1$ AU), this yields the projectile mass $m_P \sim 8.8 \times 10^2$ kg, i.e., a projectile radius $a_P \sim 0.6$ m. The flux of particles with $a \sim 0.6$ m at $R = 1$ AU is $\sim 10^{-2}$ sec^{-1} (Morfill *et al.* 1983). This implies that, for a 1-km-radius NEA, the impacting particle flux received at the surface is 3×10^{-14} sec^{-1}. Thus the collision time for an impact large enough to produce a detectable coma is $\sim 3 \times 10^{13}$ sec or 10^6 years. This timescale is slightly smaller than the dynamical lifetime of an NEA (10^7–10^8 years), suggesting that this event could only happen ~10× in an NEA lifetime, and is thus unlikely to be the principal reactivation mechanism. Our result disagrees with that of Fernandez (1990), who estimated that impact craters with diameters on the order of 100 m can be produced every few revolutions on 5-km-radius objects like P/Halley and P/Arend-Rigaux and are responsible for excavating the mantle.

2. Microbombardment erosion. Lunar rocks and regolith fragments are covered by microcraters (μm–cm in size), providing ample evidence for the erosion of the surface by micrometeoroids. How long would it take micrometeoroids to erode the mantle? The mantle of Comet Halley is estimated to be a few cm thick (e.g., Ip and Rickman 1986). If, for definiteness, we assume a mantle thickness of 0.05 m, and the lunar erosion rate ~10 Å/year (Ashworth 1978), the mantle can then be eroded away in 5×10^7 years (1–2 orders of magnitude less efficient than single impact cratering), or approximately an NEA lifetime.

ACKNOWLEDGMENTS

This work was supported in part by a Smithsonian Postdoctoral Fellowship to J. X. Luu and a grant from the National Science Foundation to D. C. Jewitt. We thank R. Millis and R. A. Brown for very valuable suggestions.

REFERENCES

A'HEARN, M. F., P. V. BIRCH, P. D. FELDMAN, AND R. L. MILLIS 1985. Comet Encke: Gas production and lightcurve. *Icarus* **64,** 1–10.

A'HEARN, M. F., H. CAMPINS, D. G. SCHLEICHER, AND R. L. MILLIS 1989. The nucleus of P/Tempel 2. *Astrophys. J.* **347,** 1155–1166.

ASHWORTH, D. G. 1978. Lunar and planetary impact erosion. In *Cosmic Dust,* (J. A. M. McDonnell, Ed.), pp. 427–526. Wiley, Chichester.

CAMPINS, H., M. F. A'HEARN, AND L. A. MCFADDEN 1987. The bare nucleus of Comet P/Neujmin 1. *Astrophys. J.* **316,** 847–857.

COCHRAN, W. D., A. L. COCHRAN, AND E. S. BARKER 1986. Spectroscopy of asteroids in unusual orbits. In *Asteroids, Comets, Meteors II* (C.-I. Lagerkvist, B. A. Lindblad, H. Lundstedt, and H. Rickman, Eds.), pp. 181–185. Uppsala Univ. Press, Uppsala.

DEGEWIJ, J. 1980. Spectroscopy of faint asteroids, satellites, and comets. *Astrophys. J.* **85,** 1403–1412.

DELSEMME, A. H. 1982. Chemical composition of cometary nuclei. In *Comets* (L. L. Wilkening, Ed.), pp. 85–130. Univ. of Arizona Press, Tucson.

DRUMMOND, J. D., AND E. K. HEGE 1989. Speckle interferometry of asteroids. In *Asteroids II* (R. P. Binzel, T. Gehrels, and M. S. Matthews, Eds.), pp. 171–191. Univ. of Arizona Press, Tucson.

FANALE, F. P., AND J. R. SALVAIL 1984. An idealized short-period comet model: Surface insolation, H_2O flux, dust flux, and mantle evolution. *Icarus* **60,** 476–511.

FERNANDEZ, J. 1990. Collisions of comets with meteoroids. In *Asteroids, Comets, and Meteors III* (C.-I. Lagerkvist, H. Rickman, B. A.

Lindblad, and M. Lindgren, Eds.), pp. 309–312. Uppsala Univ. Press, Uppsala.

FROESCHLÉ, C. 1990. Chaotic behavior of asteroidal and cometary orbits. In *Asteroids, Comets, and Meteors III* (C.-I. Lagerkvist, H. Rickman, B. A. Lindblad, and M. Lindgren, Eds.), pp. 63–76. Uppsala University Press, Uppsala.

GAULT, D. E. 1973. Displaced mass, depth, diameter, and effects of oblique trajectories for impact craters formed in dense crystalline rocks. *Moon* **6,** 32–44.

GAULT, D. E. 1974. Impact Cratering. In *A Primer in Lunar Geology* (R. Greeley and P. Schultz, Eds.), pp. 137–175. NASA Tech Memorandum TM X-62, 359.

GAULT, D. E., F. HÖRZ, AND J. B. HARTUNG 1972. Effects of microcratering on the lunar surface. *Proc. Third Lunar Sci. Conf.*, Vol. 3, pp. 2713–2734.

GRÜN, E., J. BENKHOFF, H. FECHTIG, P. HESSELBARTH, J. KLINGER, H. KOCHAN, H. KOHL, D. KRANKOWSKY, P. LÄMMERZAHL, W. SEBOLDT, T. SPOHN, AND K. THIEL 1989. Mechanisms of dust emission from the surface of a cometary nucleus. *Adv. Space Res.* **9,** 133–137.

HAHN, G., AND H. RICKMAN 1985. Asteroids in cometary orbits. *Icarus* **61,** 417–442.

HARTMANN, W. K., D. J. THOLEN, K. MEECH, AND D. P. CRUIKSHANK 1990. 2060 Chiron: Colorimetry and cometary behavior. *Icarus* **83,** 1–15.

IP, W. H., AND H. RICKMAN 1986. A comparison of nucleus surface models to space observations of Comet Halley. In *Proceedings of the Comet Nucleus Sample Return Mission Workshop,* ESA SP-249.

JEWITT, D. C. 1990. The persistent coma of Comet P/Schwassmann-Wachmann 1. *Astrophys. J.* **351,** 277–286.

JEWITT, D. C., AND J. X. LUU 1989. A CCD portrait of Comet P/Tempel 2. *Astrophys. J.* **97,** 1766–1790.

JEWITT, D. C., AND K. MEECH 1985. Rotation of the nucleus of P/Arend-Rigaux. *Icarus* **64,** 329–335.

JEWITT, D. C., AND K. MEECH 1988. Optical properties of cometary nuclei and a preliminary comparison with asteroids. *Astrophys. J.* **328,** 974–986.

JONES, T. D. 1988. *An Infrared Reflectance Study of Water in Outer Belt Asteroids: Clues to Composition and Origin.* Ph.D. Thesis, Univ. of Arizona.

KELLER, H. U., W. A. DELAMERE, W. F. HUEBNER, H. J. REITSEMA, H. U. SCHMIDT, F. L. WHIPPLE, K. WILHELM, W. CURDT, R. KRAMM, N. THOMAS, C. ARPIGNY, C. BARBIERI, R. M. BONNET, S. CAZES, M. CORADINI, C. B. COSMOVICI, D. W. HUGHES, C. JAMAR, D. MALAISE, K. SCHMIDT, W. K. H. SCHMIDT, AND P. SEIGE 1987. *Astron. Astrophys.* **187,** 807.

KÜHRT, E. 1984. Temperature profiles and thermal stresses in cometary nuclei. *Icarus* **60,** 512–521.

LEBOFSKY, L. A., M. A. FEIERBERG, A. T. TOKUNAGA, H. P. LARSON, AND J. R. JOHNSON 1981. The 1.7- to 4.2-μm spectrum of Asteroid 1 Ceres: Evidence for structural water in clay minerals. *Icarus* **48,** 453–459.

LUU, J. X., AND D. C. JEWITT 1990a. Cometary activity in 2060 Chiron. *Astrophys. J.* **100,** 913–932.

LUU, J. X., AND D. C. JEWITT 1990b. The nucleus of Comet P/Encke. *Icarus* **86,** 69–81.

MCDONNELL, J. A. M., P. L. LAMY, AND G. S. PANKIEWICZ 1991. Physical properties of cometary dust. In *Comets in the Post-Halley Era* (R. L. Newburn, Jr., M. Neugebauer, and J. Rahe, Eds.), Vol. 2, pp. 1043–1073. Kluwer, Dordrecht.

MEECH, K., AND M. BELTON 1990. *IAU Circular* 4770.

MORFILL, G. E., H. FECHTIG, E. GRÜN, AND C. K. GOERTZ 1983. Some consequences of meteoroid impact on Saturn's rings. *Icarus* **55,** 439–47.

NAKANO, S. 1989. *IAU Circular* 4752.

RICKMAN, H. 1988. Relations between small bodies: Discussion. *Celestial Mechanics* **43,** 413–416.

RICKMAN, H., B. Å. S. GUSTAFSON, AND J. A. FERNANDEZ 1990. Model calculations of mantle formation on comet nuclei. In *Asteroids, Comets, and Meteors III* (C.-I. Lagerkvist, H. Rickman, B. A. Lindblad, and M. Lindgren, Eds.), pp. 423–426. Uppsala Univ. Press, Uppsala.

SCHLOERB, F. P., W. M. KINZEL, D. A. SWADE, AND W. M. IRVINE 1986. HCN production from Comet Halley. In *20th ESLAB Symposium on the Exploration of Halley's Comet* (B. Battrick, E. J. Rolfe, R. Reinhard, Eds.), pp. 577–581. ESA Publ. Div., ESTEC, Noordwijk.

SPINRAD, H., J. STAUFFER, AND R. L. NEWBURN 1979. Optical spectrophotometry of Comet Tempel 2 far from the Sun. *Publ. Astron. Soc. Pac.* **92,** 707–711.

WEISSMAN, P. R., M. F., A'HEARN, L. A. MCFADDEN, AND H. RICKMAN 1989. Evolution of comets into asteroids. In *Asteroids II* (R. P. Binzel, T. Gehrels, and M. S. Matthews, Eds.), pp. 880–920. Univ. of Arizona Press, Tucson.

WISDOM, J. 1987. Chaotic dynamics in the Solar System. *Icarus* **72,** 241–275.